Article

Synthesis of Sulfonic Acid-Functionalized g-C$_3$N$_4$/BiOI Bifunctional Heterojunction for Enhanced Photocatalytic Removal of Tartrazine and PEC Oxygen Evolution Reaction

Sridharan Balu [1,2,†], Harikrishnan Venkatesvaran [1,†], Chien-Chih Wang [1], Joon Ching Juan [3] and Thomas Chung-Kuang Yang [1,2,*]

[1] Department of Chemical Engineering and Biotechnology, National Taipei University of Technology, No. 1, Section 3, Zhongxiao East Road, Da'an District, Taipei City 10608, Taiwan; bsridharanbsc.12@gmail.com (S.B.); harikrishnan.osv@gmail.com (H.V.); bobobo456123@gmail.com (C.-C.W.)

[2] Precision Analysis and Materials Research Center, National Taipei University of Technology, No. 46, Section 3, Zhongxiao E. Road, Da'an District, Taipei City 106083, Taiwan

[3] Nanotechnology and Catalysis Research Center (NANOCAT), Institute for Advanced Studies, University of Malaya, Kuala Lumpur 50603, Malaysia; jcjuan@um.edu.my

* Correspondence: ckyang@mail.ntut.edu.tw; Tel.: +886-02-2771-2171 (ext. 2533)

† These authors contributed equally to this work.

Abstract: A Z-scheme heterojunction photo(electro)catalyst was fabricated by coupling sulfonic acid-modified graphitic carbon nitride (SA-g-CN) with bismuth oxyiodide (BiOI). The SA-g-CN component was prepared via wet-impregnation, while BiOI was synthesized through a hydrothermal method. Comprehensive characterization elucidated the structural and morphological properties of the resulting composite. The SA-g-CN/BiOI exhibited exceptional performance in both photocatalytic degradation of tartrazine (TTZ) and photoelectrochemical oxygen evolution reaction (OER). Notably, 98.26% TTZ removal was achieved within 60 min of irradiation, while an OER onset potential of 0.94 V (vs. Ag/AgCl) and a high photocurrent density of 6.04 mA were recorded under AM 1.5G illumination. Band energy calculations based on Mott–Schottky measurements confirmed the formation of a Z-scheme heterojunction, which facilitated efficient charge separation and transfer, thereby enhancing catalytic activity. These findings establish the SA-g-CN/BiOI composite as a promising candidate for sustainable energy generation and environmental remediation applications.

Keywords: sulfonic acid; g-C$_3$N$_4$; BiOI; heterojunction; tartrazine; photodegradation; water-splitting

1. Introduction

Semiconductor photocatalysis presents a multifaceted approach to addressing pressing global challenges. By harnessing solar energy, these materials can initiate the decomposition of water into hydrogen and oxygen, providing a sustainable pathway to clean fuel production [1–4]. Concurrently, they can effectively degrade organic pollutants within aquatic environments through the generation of reactive oxygen species. This dual functionality underscores the potential of semiconductor photocatalysis as a pivotal technology for both energy generation and environmental remediation [5–7]. Tartrazine, a synthetic azo dye ubiquitously employed in food products, poses significant environmental challenges due to its recalcitrance and potential toxicity [8–10]. Conventional wastewater treatment processes often prove ineffective in removing this contaminant. Photocatalysis, a green technology, presents a promising avenue for the degradation of such persistent organic pollutants. This process leverages light energy to generate highly reactive species, such as hydroxyl radicals, capable of oxidizing organic compounds into harmless byproducts [11–14].

Graphitic carbon nitride (g-C$_3$N$_4$) and bismuth oxyiodide (BiOI), distinguished by their favorable band structures and visible light absorption, have emerged as prospective photocatalysts. A non-toxic polymeric semiconductor, g-C$_3$N$_4$ has an optical bandgap of

approximately 2.5–2.7 eV. It exhibits several desirable properties, including high temperature and chemical stability, a wide range of visible-light absorption, a suitable surface for immobilizing other materials, and the potential for bandgap tuning. However, g-C$_3$N$_4$ also suffers from limitations such as a rapid charge recombination rate and limited surface area in its bulk form [15]. Nevertheless, their practical application is hindered by limitations such as rapid charge recombination and suboptimal photocatalytic efficiency [16–18]. To address these challenges, strategies including metal/nonmetal doping, heterojunction formation and surface functionalization have been explored.

Sulfonic acid functionalization of g-C$_3$N$_4$ is anticipated to introduce additional active sites, enhance the adsorption of organic pollutants, and facilitate charge carrier mobility through the creation of hydrophilic domains [19–21]. The augmented hydrophilicity is expected to promote the adsorption and subsequent degradation of organic contaminants, while improved charge separation can facilitate efficient electron transfer and the generation of reactive oxygen species essential for pollutant degradation [22]. Beyond environmental remediation, the pursuit of sustainable energy production is paramount. Photoelectrochemical water splitting, a process that harnesses solar energy to decompose water into hydrogen and oxygen, offers a promising pathway to renewable energy generation. This process relies on photocatalysts to absorb sunlight, generate charge carriers, and drive the oxidation of water at the anode (OER) and the reduction of protons at the cathode (HER) [23–26].

In this work, we investigated the synthesis and characterization of a novel sulfonic acid-functionalized SA-g-CN/BiOI heterojunction catalyst for the effective degradation of tartrazine under visible light irradiation. Additionally, the photoelectrochemical oxygen evolution reaction performance of the synthesized catalyst will be assessed to evaluate its potential for solar energy conversion. The as-synthesized catalysts were analyzed through various spectroscopic and microscopic techniques. This multifaceted approach aims to develop a multifunctional material exhibiting enhanced efficiency and stability for both environmental remediation and energy production applications.

2. Results and Discussion

Field-emission scanning electron microscopy (FESEM) was employed to characterize the surface morphology of the synthesized materials. The as-prepared g-C$_3$N$_4$ (g-CN) exhibited a typical 2D lamellar sheet-like structure (Figure 1a), providing a suitable platform for the subsequent integration of semiconductor nanoparticles. Energy-dispersive X-ray (EDX) spectroscopy confirmed the composition of g-CN, with a C/N atomic ratio of 0.82, approximating the theoretical value of 0.75 (Figure 1a'). Sulfonic acid functionalization did not alter the fundamental 2D morphology of g-CN (SA-g-CN) (Figure 1b). The successful introduction of -SO$_3$H groups was verified by EDX analysis (Figure 1b'). BiOI exhibited a distinctive thin nanoplate structure (Figure 1c), as revealed by FESEM. The corresponding elemental composition is presented in Figure 1c'. The g-CN/BiOI composite displayed a homogeneous distribution of BiOI nanoparticles on the g-C$_3$N$_4$ surface (Figure 1d). EDX analysis confirmed the presence of all constituent elements (Figure 1d'). The SA-g-CN/BiOI nanocomposite maintained the morphological characteristics of g-CN/BiOI (Figure 1e), emphasizing the role of the 2D lamellar structure of SA-g-CN. EDX analysis of SA-g-CN/BiOI (Figure 1e') corroborated the presence of all expected elements. Additionally, elemental mapping analysis of SA-g-CN/BiOI (Figure 1f) visually confirms the successful sulfonic acid functionalization, the uniform distribution of BiOI on the g-C$_3$N$_4$ surface, and the formation of a heterojunction composite.
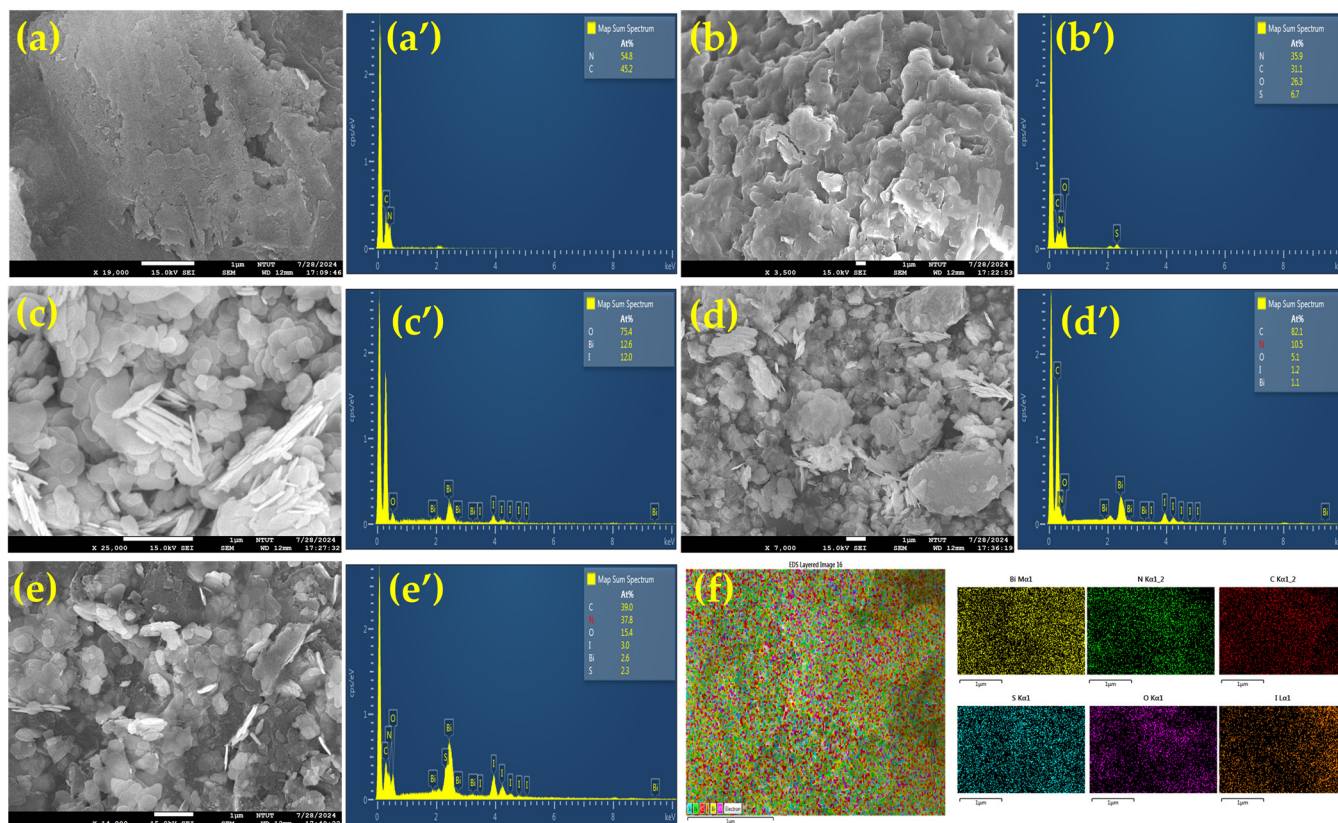
Figure 1. FESEM images and EDX spectra of as-synthesized g-CN (**a**,**a′**), sulfonic acid-functionalized AS-g-CN (**b**,**b′**), BiOI (**c**,**c′**), g-CN/BiOI (**d**,**d′**), and AS-g-CN/BiOI (**e**,**e′**). Elemental mapping of AS-g-CN/BiOI heterojunction composite (**f**).

X-ray diffraction (XRD) (Figure 2a) analysis revealed characteristic peaks at approximately 13.0° and 27.6° in both pristine g-CN and SA-g-CN, corresponding to the (100) and (002) crystal planes, respectively. These peaks are attributed to the in-plane structural packing and interlayer stacking of the graphitic g-CN structure (JCPDS No. 87-1526) [27]. While CN-SAF exhibited a similar diffraction pattern, a reduction in the intensity of the 27.6° peak was observed, indicating an increased interlayer spacing due to the incorporation of surface-functionalized sulfonic groups. XRD patterns of pure BiOI exhibited characteristic peaks at 9.65°, 29.6°, 31.6°, 37.0°, 39.3°, 45.9°, 51.3°, 55.1°, 60.2°, and 61.5°, corresponding to the (001), (102), (110), (103), (004), (200), (114), (212), (115), and (204) planes, respectively. These diffraction patterns confirmed the formation of a tetragonal phase (space group *P4/nmm*) for the BiOI nanoplates (JCPDS No. 96-434-1501) [28]. The XRD patterns of both g-CN/BiOI and SA-g-CN/BiOI composites displayed characteristic peaks corresponding to both SA-g-CN (marked as spades) and BiOI (marked as diamonds), providing evidence for the successful formation of heterojunction structures.

Fourier transform infrared spectroscopy (FTIR) investigation (Figure 2b) was employed to identify the functional groups and chemical bonds present in the synthesized nanomaterials. The FTIR spectra of pristine g-CN and SA-g-CN, recorded in the 400–4000 cm^{-1} region, exhibited characteristic vibrational bands. Pure g-CN displayed characteristic absorption bands between 1200 and 1600 cm^{-1}, attributed to the C–N heterocycles within the heptazine units. A sharp peak at 807 cm^{-1} corresponded to the stretching vibrations of C–N–C moieties in the triazine ring [29]. In contrast, the spectrum of SA-g-CN revealed additional peaks at 615 and 796 cm^{-1}, assigned to the bending vibrations of –SO and C–N–S groups, respectively, indicating the successful incorporation of sulfonic acid functional groups. Furthermore, the presence of surface sulfonic groups was confirmed by vibrational bands at 968 and 1124 cm^{-1}. A broad absorption band observed between 3060 cm^{-1} and

3300 cm^{-1} was attributed to the stretching vibrations of –NH, =NH, and –OH groups originating from uncreated amino groups and adsorbed water [30]. On the other hand, the FTIR analysis revealed a characteristic peak at 571.5 cm^{-1} attributed to the symmetric stretching vibration of the Bi-O bond in BiOI. Additionally, strong absorption bands were observed within the 1300–1700 cm^{-1} region, likely associated with the presence of organic impurities or adsorbed species. A broad and intense peak centered around 3350 cm^{-1} indicated the presence of adsorbed water molecules, with contributions from both bending ($\sim$1650 cm^{-1}) and stretching ($\sim$3500–3000 cm^{-1}) vibrational modes of hydroxyl groups (–OH) [31]. Correspondingly, the FTIR spectra of g-CN/BiOI and SA-g-CN/BiOI exhibit the combined vibrational bands of SA-g-CN and BiOI, which confirms the excellent formation of heterojunction composite.
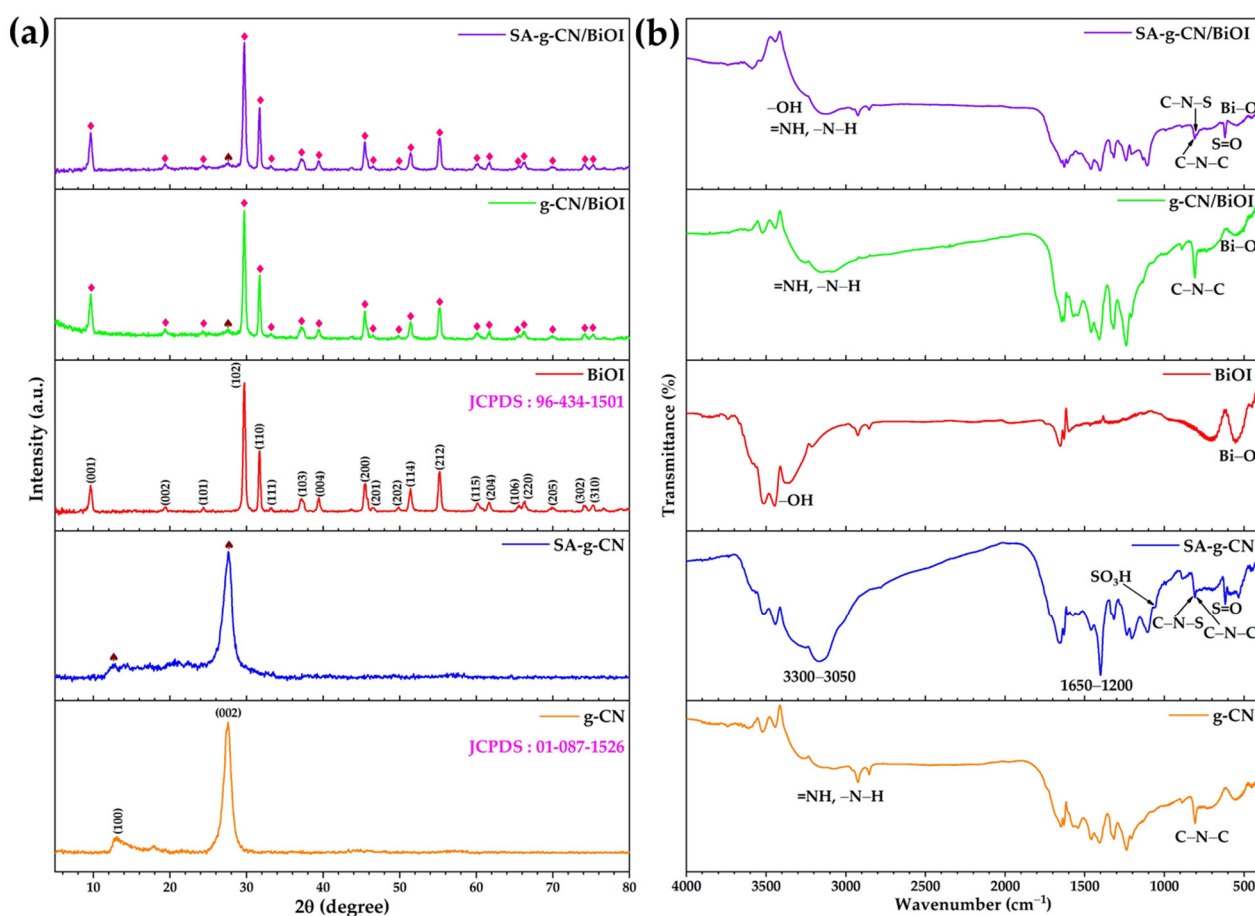

Figure 2. X-ray diffraction patterns (**a**) and Fourier-transform infrared spectra (**b**) of g-CN, sulfonic acid-functionalized SA-g-CN, BiOI, g-CN/BiOI, and SA-g-CN/BiOI.

X-ray photoelectron spectroscopy (XPS) was employed to investigate the chemical environment and bonding interactions within the catalytic nanocomposites. Figure 3a presents survey spectra (0 to 1000 eV) of SA-g-CN, BiOI, and SA-g-CN/BiOI, confirming the presence of the expected elements. High-resolution spectra of C 1s, N 1s, Bi 4f, O 1s, and I 3d are shown in Figure 3b–f. Deconvolution of the C 1s spectra from pristine SA-g-CN and SA-g-CN/BiOI revealed two peaks at 284.76 and 287.9 eV, attributed to C–C and N–C=N bonds, respectively. Similarly, the N 1s spectra exhibited peaks at 398.52 and 400.21 eV, corresponding to pyridinic and graphitic nitrogen. Compared to the pristine SA-g-CN, the C 1s and N 1s peaks in SA-g-CN/BiOI shifted to higher binding energies. This suggests an increase in electron density/cloud or a change in the electronic structure of SA-g-CN upon contact with BiOI under light irradiation, possibly due to interfacial charge transfer. Further XPS analysis of the S 2p region (Figure S1) revealed two distinct peaks at

164.79 and 168.11 eV, indicative of –SH and –SO$_3$H groups, respectively, confirming the successful sulfonic acid functionalization of g-CN. Due to spectral overlap with bismuth, the S 2p spectrum of SA-g-CN/BiOI could not be clearly distinguished. The Bi 4f spectrum exhibited two prominent peaks at 158.13 and 163.54 eV, corresponding to the Bi^{3+} states of Bi 4f7/2 and Bi 4f5/2. The O 1s spectrum of SA-g-CN was deconvoluted into two peaks at 531.55 and 533.46 eV, attributed to the –SO$_3$H and –OH groups of the sulfonic acid functional groups. In SA-g-CN/BiOI, the O 1s spectrum showed peaks at 529.94 and 532.06 eV, corresponding to Bi–O and surface-bound hydroxyl (–OH) groups, respectively. The I 3d spectrum of BiOI displayed two significant peaks at 619.08 and 630.57 eV, attributed to I 3d5/2 and I 3d3/2. The observed higher binding energy shifts for Bi 4f and I 3d in the SA-g-CN/BiOI heterojunction catalyst suggest an increased electron density, likely due to enhanced photogenerated charge transfer across the heterojunction interface.
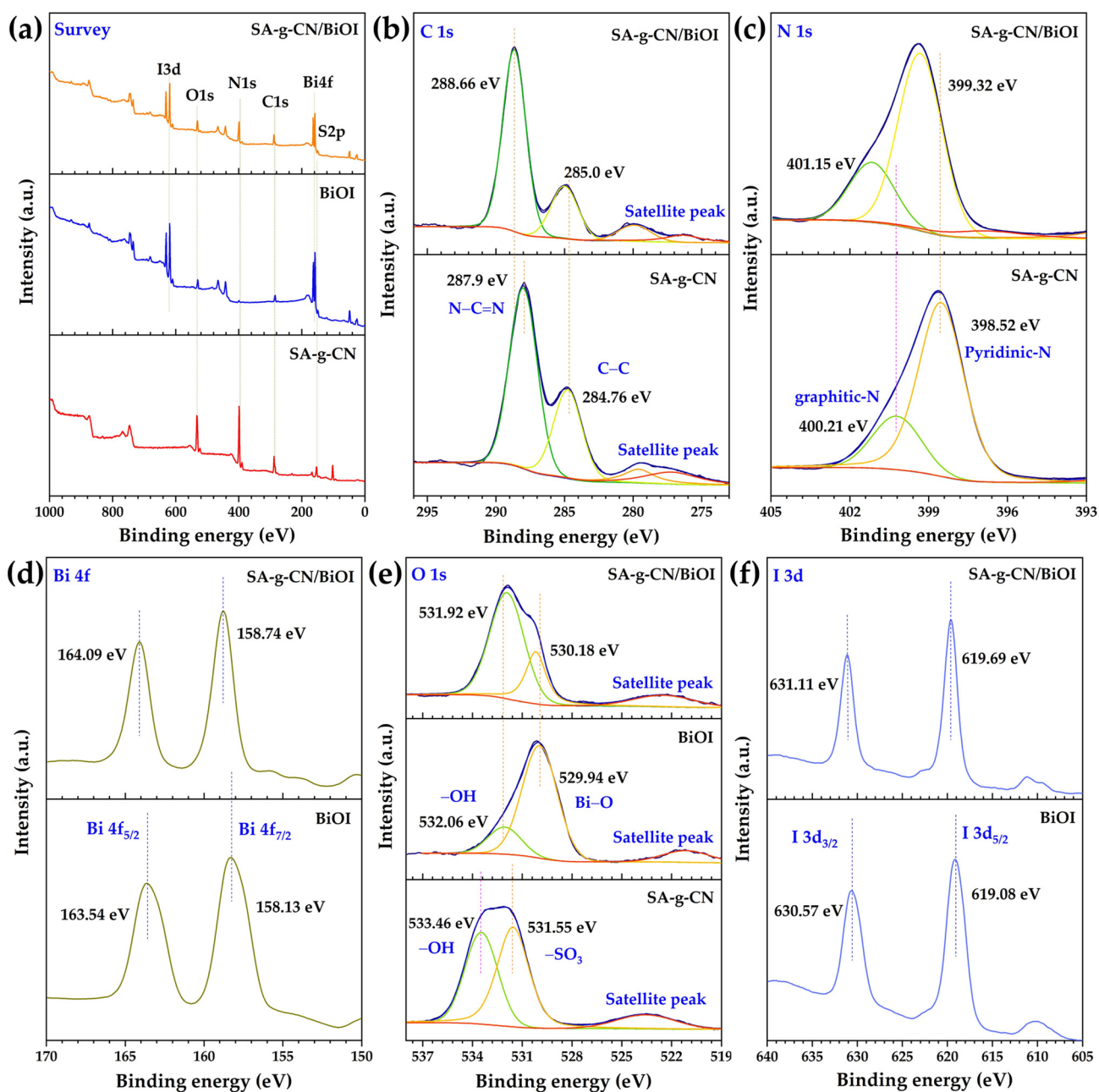

Figure 3. XPS survey spectra (**a**), core-level spectra of C 1s (**b**), N 1s (**c**), Bi 4f (**d**), O 1s (**e**), and I 3d (**f**) of SA-g-CN, BiOI, g-CN/BiOI, and SA-g-CN/BiOI.

The optical absorption properties of the prepared samples were investigated using UV-Vis diffuse reflectance spectroscopy (UV-DRS) (Figure 4a). Both pristine g-CN and SA-g-CN exhibited absorption edges at approximately 469.8 nm, indicating a primary response to the UV region of the spectrum. In contrast, BiOI demonstrated enhanced visible light absorption with a band edge centered at approximately 690 nm. Interestingly, the g-CN/BiOI and SA-g-CN/BiOI composites displayed red-shifted absorption edges, reaching approximately 685 nm and 715 nm, respectively. These results suggest that the incorporation of BiOI significantly improved visible light absorption and potentially reduced bandgap energies, which are essential parameters for efficient photo(electro)catalytic processes.
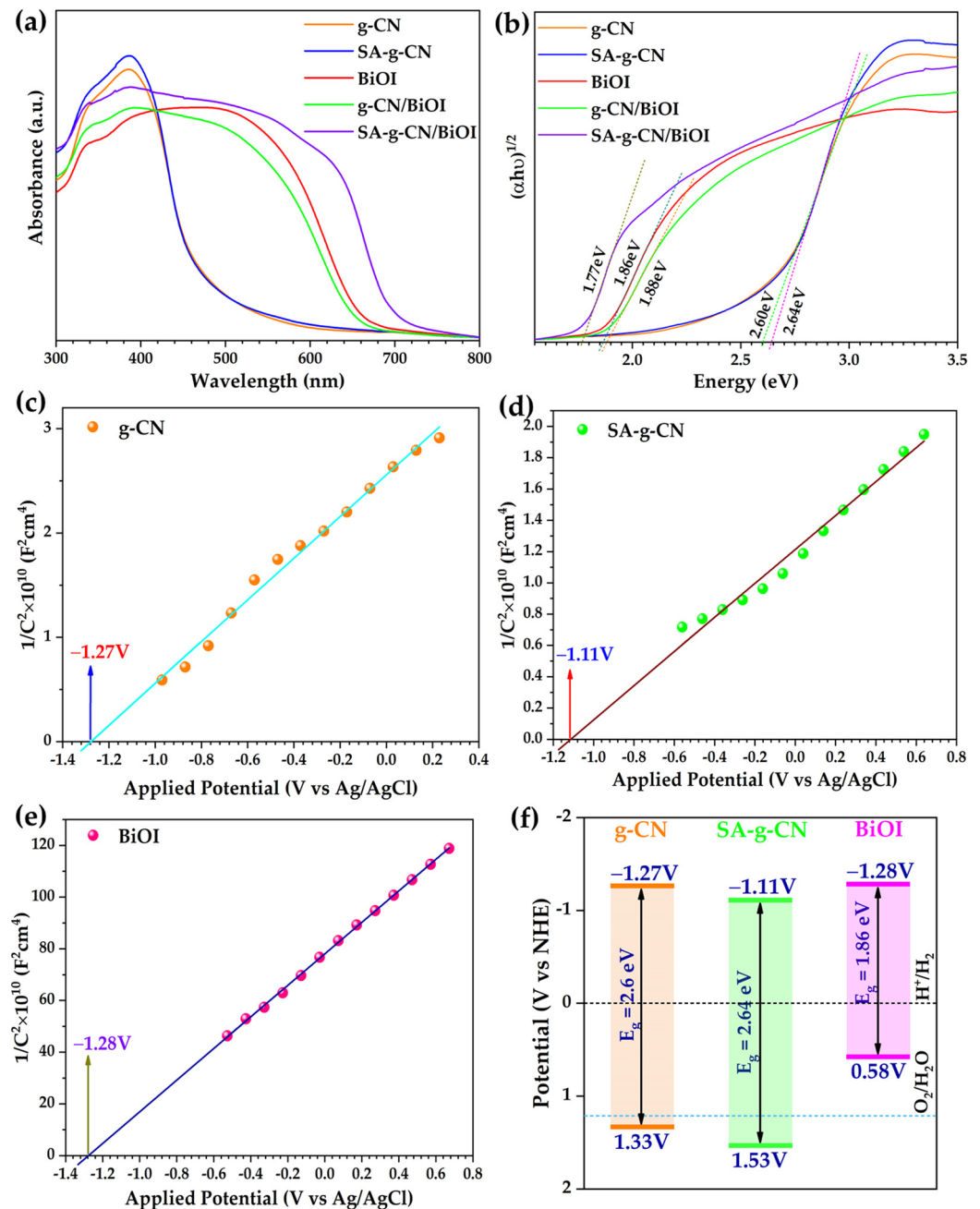

Figure 4. UV-diffuse reflectance spectra (**a**), Tauc plots (**b**), electrochemical Mott–Schottky curves of g-CN (**c**), SA-g-CN (**d**), BiOI (**e**), and band energy diagram of the pristine materials (**f**).

The bandgap energy (E_g) was estimated through Tauc plots (Figure 4b) constructed using the Kubelka–Munk function (Equation (1)) [32]. This equation relates the absorption coefficient (α) to the photon energy (hν):

$$\alpha h\nu = A(h\nu - E_g)^n \tag{1}$$

where A is a proportionality constant, h = Planck's constant, E_g = bandgap energy, and n is a transition coefficient with values of 1/2 for direct allowed transitions and 2 for indirect allowed transitions. The calculated bandgap energies (E_g) for g-CN, SA-g-CN, BiOI, g-CN/BiOI, and SA-g-CN/BiOI were determined to be 2.64, 2.60, 1.86, 1.88, and 1.77 eV, respectively. The substantial reduction in the E_g of the SA-g-CN/BiOI heterojunction suggests a synergistic interplay between the electronic and optical properties of SA-g-CN and BiOI, potentially contributing to enhanced photo(electro)catalytic activities.

The electrochemical properties of the semiconductor materials were characterized through Mott–Schottky analysis (Figure 4c–e) in the presence of 0.1 M Na_2SO_4. The flat-band potential (E_{fb}) of the semiconductor materials can be determined using the Mott–Schottky plot ($1/C^2$ vs. potential) by extrapolating the linear portion to the point where it intercepts the X-axis ($V_{fb} + kT/e$) (Equation (2)). This E_{fb} value also corresponds to the Fermi level since band bending becomes negligible at the E_{fb} potential. In n-type and p-type semiconductors, the Fermi level aligns with the conduction band (E_{cb}) and valence band (E_{vb}) edges, respectively [33].

$$1/C^2 = (2/(\varepsilon\varepsilon_0 eN_d)) \times (V - V_{fb} - kT/e) \tag{2}$$

$$E_{vb} = E_{cb} + E_g \tag{3}$$

Mott–Schottky analysis revealed flat band potentials (E_{fb}) of –1.27, –1.11, and –1.28 V for g-CN, SA-g-CN, and BiOI, respectively. Valence band potentials (E_{vb}) were subsequently calculated using Equation (3), resulting in values of +1.33, +1.53, and +0.58 V, respectively. Based on the determined E_g, E_{cb}, and E_{vb} values from DRS-Tauc and Mott–Schottky analyses, the corresponding band energy diagrams are presented in Figure 4f.

Photoluminescence (PL) spectroscopy was employed to investigate charge carrier dynamics, specifically photoexcitation and recombination processes (Figure 5a). Pristine g-CN exhibited an emission peak centered at approximately 475 nm, while sulfonic acid-functionalized SA-g-CN displayed a blue-shifted emission at around 445 nm. PL emission intensity is directly correlated with the rate of charge carrier recombination during photocatalytic and photoelectrochemical processes. Notably, g-CN/BiOI and SA-g-CN/BiOI composites demonstrated significantly reduced PL intensities compared to their pristine counterparts, indicating suppressed charge recombination due to the formation of heterojunction interfaces. This phenomenon is anticipated to contribute to enhanced photoelectrochemical performance.

The photocatalytic performance of the SA-g-CN/BiOI heterojunction catalyst was evaluated by monitoring the degradation of tartrazine (TTZ), a synthetic food dye, under simulated solar light irradiation (300 W Xenon lamp, AM 1.5G filter, 100 mW/cm^2). Approximately 0.02 g of catalyst was dispersed in 100 mL of a 10 mg/L TTZ aqueous solution. Prior to irradiation, the mixture was stirred in the dark to establish adsorption–desorption equilibrium. The progress of TTZ degradation was monitored via UV-Vis spectroscopy at 10 min intervals. Figure 5b presents the TTZ concentration as a function of irradiation time (C/C_0), revealing a 98.26% removal efficiency within 60 min. This represents a 3.06, 2.14, 4.48, 1.56, and 16.48-fold enhancement compared to pristine g-CN (32.09%), SA-g-CN (45.91%), BiOI (21.9%), g-CN/BiOI (62.65%), and photolysis (32.09%), respectively. The superior photocatalytic activity of SA-g-CN/BiOI is attributed to a synergistic effect between SA-g-CN and BiOI. The sulfonic group acts as an electron trap, promoting electron transfer to the catalyst surface and extending the lifetime of charge carriers. Moreover, the formation of a heterojunction interface effectively suppresses charge recombination, thereby enhancing overall photocatalytic efficiency.
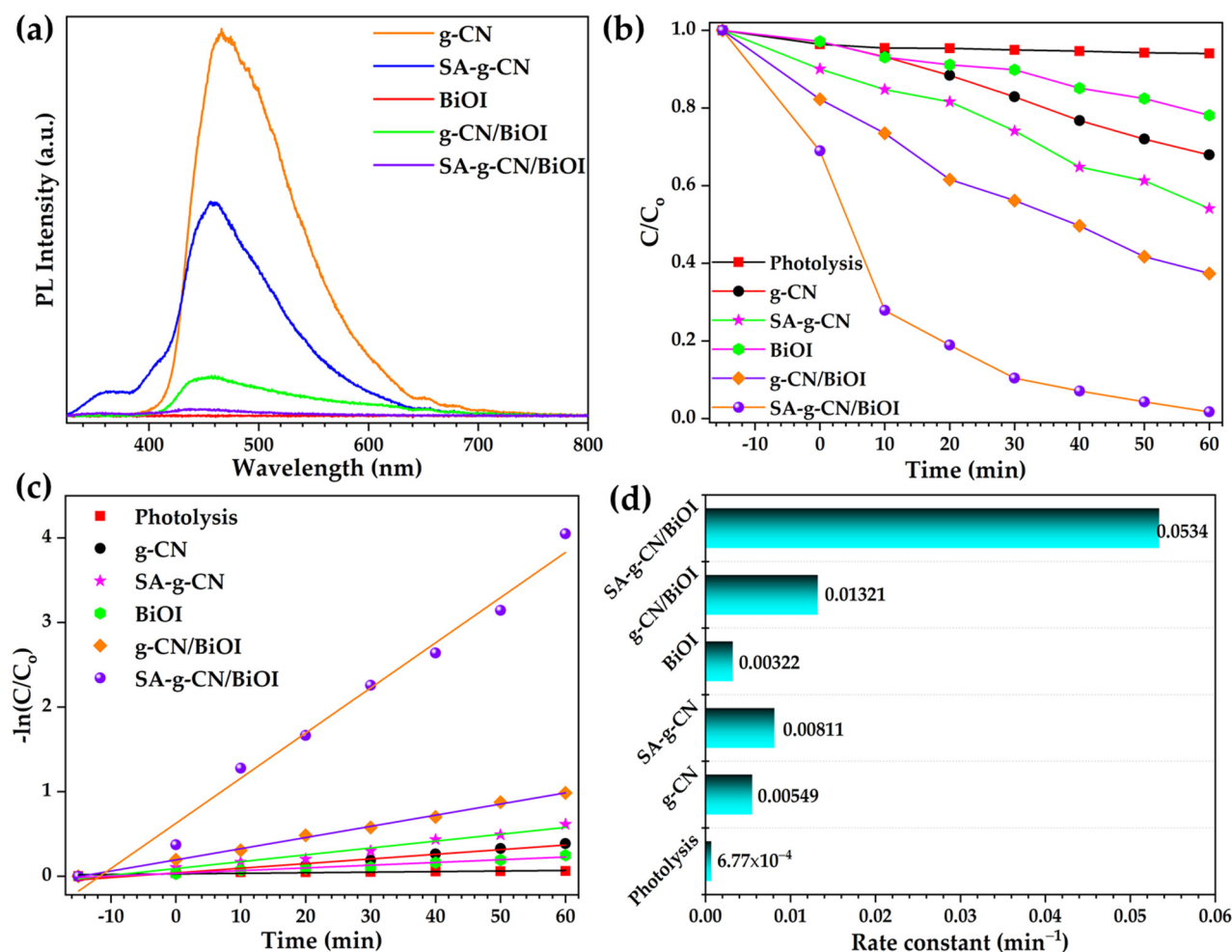
Figure 5. Photoluminescence (PL) spectra (**a**), tartrazine concentration vs. degradation time (C/C$_0$) plot (**b**), −lnC/C$_0$ kinetics plot (**c**), and rate constant vs. different catalysts (**d**).

The kinetics of TTZ photodegradation was assessed by plotting −ln(C/C$_0$) against degradation time (t) (Figure 5c). The linear relationship observed for the SA-g-CN/BiOI system indicates pseudo-first-order reaction kinetics, conforming to the equation −ln(C/C$_0$) = kt. The calculated rate constants (k) for TTZ photodegradation in the presence of various catalysts are presented in Figure 5d. SA-g-CN/BiOI exhibited the highest rate constant (0.0534 min^{-1}), surpassing those of g-CN (0.00549 min^{-1}), SA-g-CN (0.00811 min^{-1}), BiOI (0.00322 min^{-1}), and g-CN/BiOI (0.0132 min^{-1}). Importantly, all systems demonstrated excellent correlation coefficients (R^2) of unity, further supporting the pseudo-first-order kinetic model.

Electrochemical impedance spectroscopy (EIS) and transient photocurrent (TPC) measurements were employed to investigate charge transfer resistance (R$_{ct}$) and transient photoresponse, respectively. EIS spectra (Figure 6a) revealed a significantly lower R$_{ct}$ value of 9.1 Ω for SA-g-CN/BiOI compared to g-CN (44.5 Ω), SA-g-CN (15.1 Ω), BiOI (50.6 Ω), and g-CN/BiOI (90.2 Ω). The reduced R$_{ct}$ in SA-g-CN/BiOI is attributed to efficient charge transfer facilitated by the heterojunction interface and the electron-trapping capability of the sulfonic group, promoting facile charge transport across the photoanode–electrolyte interface, and enhancing photoelectrochemical (PEC) performance. TPC measurements (Figure 6b) were conducted via chronoamperometry (i-t) in 0.1 M NaOH under intermittent light conditions (10 s on/off cycles) to evaluate charge carrier dynamics. The SA-g-CN/BiOI nanocomposite exhibited the highest photocurrent response, corroborating the formation of an efficient heterojunction and the suppression of charge recombination.
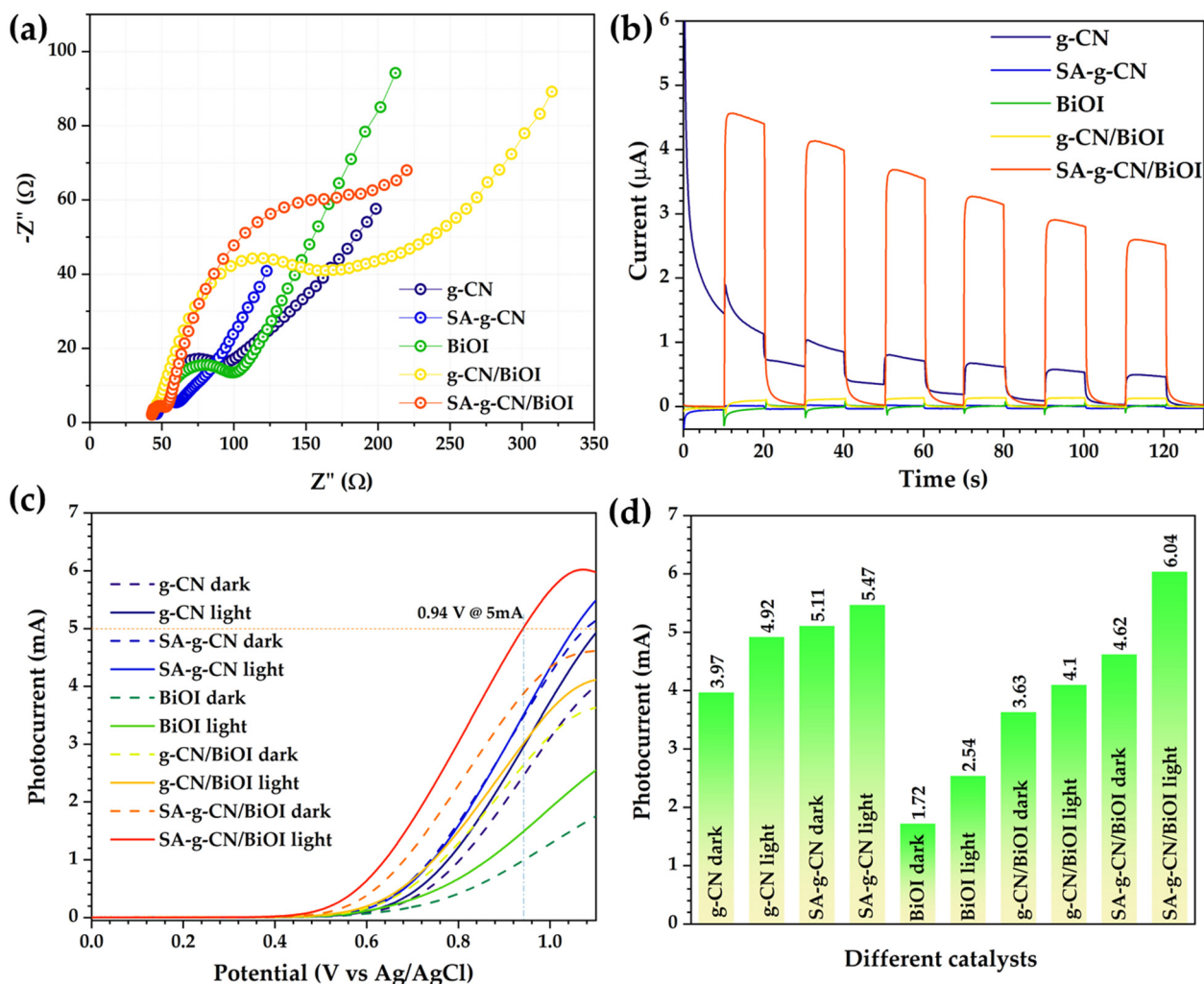
Figure 6. Electrochemical impedance (EIS) spectra (**a**), transient photocurrent curves (**b**), photoelectrochemical oxygen evolution reaction LSV curves in the presence of 0.1 M Na_2SO_4 with Na_2SO_3 hole scavenger under AM 1.5G illumination (**c**), and histogram of photocurrent vs. different catalyst (**d**).

The photoelectrochemical (PEC) water oxidation performance of the catalysts was assessed via linear sweep voltammetry (LSV) to evaluate oxygen evolution reaction (OER) activity. Figure 6c presents LSV polarization curves recorded in 0.1 M Na_2SO_4 electrolyte containing Na_2SO_3 as a hole scavenger under simulated AM 1.5G illumination. A discernible enhancement in photocurrent was observed for all catalysts compared to their respective dark currents. Notably, the SA-g-CN/BiOI heterojunction exhibited the highest photocurrent density of 6.04 mA, surpassing those of g-CN (4.92 mA), SA-g-CN (5.47 mA), BiOI (2.54 mA), and g-CN/BiOI (4.1 mA). Moreover, the SA-g-CN/BiOI Z-scheme system demonstrated a lower onset potential of 0.94 V at a current density of 5 mA compared to the other catalysts. A comparative summary of photocurrent densities for all materials is provided in Figure 6d. The formation of a Z-scheme heterojunction interface between SA-g-CN and BiOI is pivotal in augmenting photocatalytic efficiency. This interfacial region serves as an effective charge separation center, mitigating recombination losses and prolonging the lifetime of photogenerated charge carriers.

The recyclability of the SA-g-CN/BiOI Z-scheme composite was assessed through five consecutive photocatalytic degradation cycles of TTZ (Figure 7a). A slight decrease in degradation efficiency from 98.31% to 93.24% was observed after the fifth cycle, primarily attributed to catalyst loss during recovery. Nevertheless, the overall retention of 93.24% degradation efficiency underscores the robust photocatalytic stability of the composite. To elucidate the dominant reactive species involved in TTZ degradation, radical trapping

experiments were conducted using silver nitrate (SN), triethanolamine (TEOA), acrylic acid (AA), and isopropanol (IPA) as scavengers for electrons (e^-), holes (h^+), superoxide radicals ($\bullet O_2^-$), and hydroxyl radicals ($\bullet OH$), respectively (Figure 7b). The addition of AA resulted in a significant reduction of degradation efficiency to 51.72%, indicating that superoxide radicals ($\bullet O_2^-$) play a predominant role in TTZ removal, followed by holes (h^+), hydroxyl radicals ($\bullet OH$), and electrons (e^-).
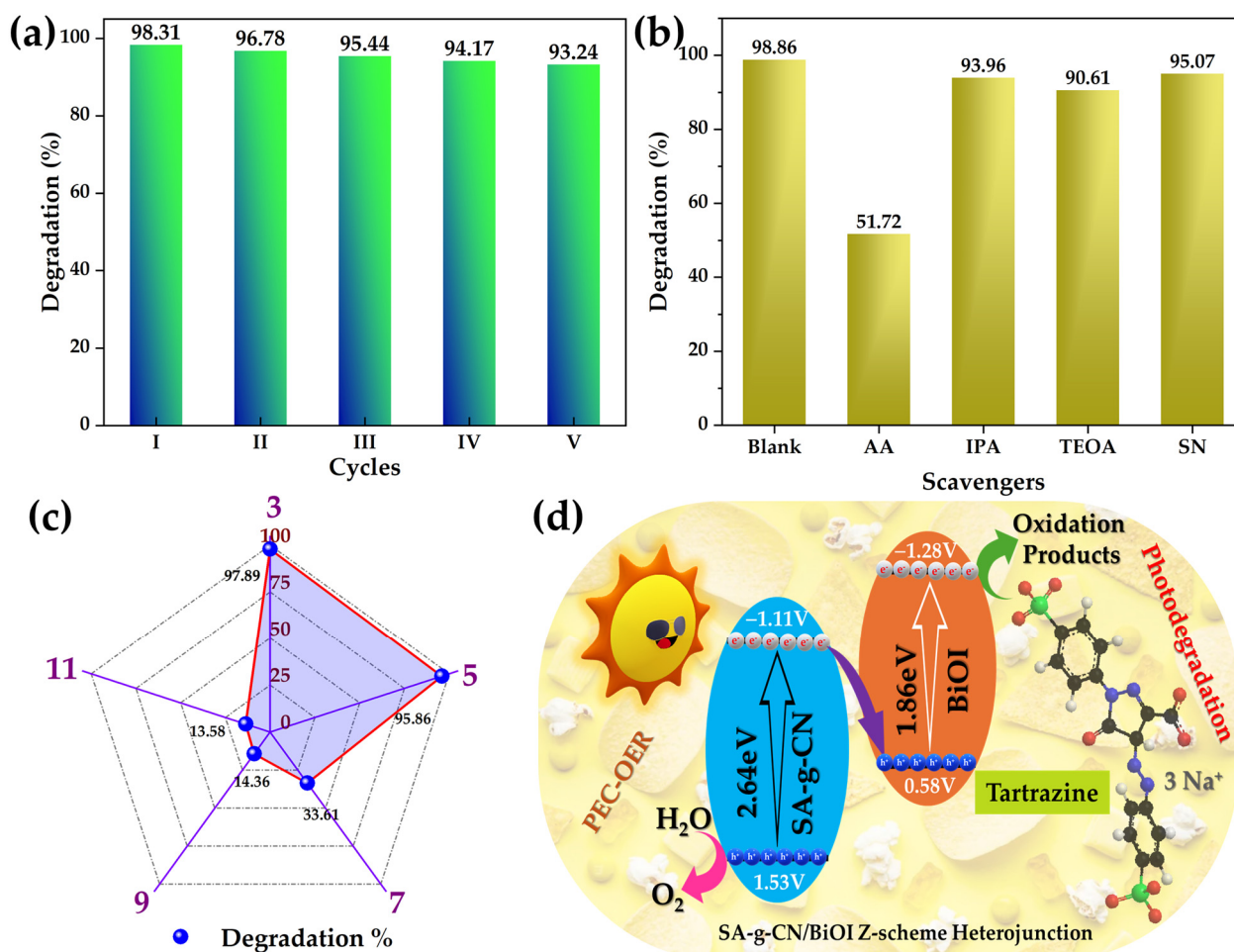

Figure 7. Recycling stability of SA-g-CN/BiOI heterojunction towards TTZ photodegradation (**a**), active species scavenging experiment (**b**), photodegradation of TTZ under different pHs (**c**), and plausible photo(electro)catalytic mechanism over SA-g-CN/BiOI Z-scheme heterojunction (**d**).

To assess the crystalline and chemical stability of the recycled catalysts, X-ray diffraction (XRD) and Fourier-transform infrared (FTIR) spectroscopy were employed. Figure S2a presents the XRD patterns of the recycled SA-g-CN/BiOI nanocomposite catalyst after five successive reaction cycles, demonstrating excellent crystalline stability. Figure S2b shows the FTIR spectrum of the recycled catalyst, indicating minimal changes in the chemical composition, thus confirming its robust chemical stability. These findings collectively suggest that the as-synthesized SA-g-CN/BiOI photocatalytic heterojunction exhibits remarkable stability under repeated reaction conditions. The structural integrity of the recycled SA-g-CN/BiOI heterojunction catalyst was assessed via FESEM analysis (Figure S3a,b), which confirmed the preservation of the composite's morphology and structural stability after five consecutive catalytic cycles. This observation underscores the catalyst's robust nature and its potential for long-term application.

The photodegradation of TTZ was evaluated under varying pH conditions (Figure 7c). The results indicate that TTZ photodegradation decreased with increasing pH from 3 to 11.

At pH 3, a maximum TTZ photodegradation of 97.89% was achieved, while photodegradation decreased to 95.86% at pH 5. For pH 7, 9, and 11, TTZ removal percentages were 33.61%, 14.36%, and 13.58%, respectively. These findings suggest that TTZ adsorption onto the SA-g-CN/BiOI catalyst surface is enhanced at lower pH values due to increased protonation, leading to stronger electrostatic interactions. Conversely, at higher pH values, the decrease in protonation reduces TTZ adsorption, resulting in lower photodegradation efficiency.

A proposed photo(electro)catalytic mechanism for the SA-g-CN/BiOI heterojunction is illustrated in Figure 7d. Bandgap energies (E_g), conduction band (CB), and valence band (VB) potentials (E_{cb} and E_{vb}) were determined through DRS and Mott–Schottky measurements. Calculated E_{cb} and E_{vb} values for SA-g-CN were −1.11 V and +1.53 V, respectively, while those for BiOI were −1.28 V and +0.58 V. Notably, the CB of SA-g-CN is positioned at a less negative potential compared to that of BiOI, while its VB is situated at a more positive potential.

Upon light irradiation, photogenerated electrons in the CB of SA-g-CN migrate to the VB of BiOI, recombining with holes. Consequently, electrons accumulate in the CB of BiOI, while holes concentrate in the VB of SA-g-CN. This spatial separation of charge carriers effectively inhibits recombination, promoting their participation in redox reactions. The observed Z-scheme charge transfer mechanism within the SA-g-CN/BiOI heterojunction is instrumental in enhancing photocatalytic and photoelectrochemical performance.

3. Materials and Methods

3.1. Materials

Dicyandiamide ($C_2H_4N_4 \geq 99\%$), sulfuric acid ($H_2SO_4 \geq 99.999\%$), bismuth nitrate pentahydrate ($Bi(NO_3)_3 \cdot 5H_2O \geq 99.999\%$), potassium iodide ($KI \geq 99.0\%$), polyvinyl pyrrolidine (PVP-10,000 MW), methanol ($CH_3OH \geq 99.8\%$), isopropanol ($C_3H_8O \geq 99.5\%$), silver nitrate ($AgNO_3 \geq 99.999\%$), acrylic acid ($C_3H_4O_2 \geq 99\%$), triethanolamine (TEOA $\geq 98\%$), sodium sulfate ($Na_2SO_4 \geq 99.0\%$), sodium sulfite ($Na_2SO_3 \geq 98.0\%$), sodium hydroxide (NaOH $\geq 97.0\%$), potassium chloride ($KCl \geq 99.0\%$), potassium ferri/ferrocyanide ($K_3[Fe(CN)_6] \geq 99.0\%/K_4[Fe(CN)_6] \cdot 3H_2O \geq 98.5\%$), tartrazine ($C_{16}H_9N_4Na_3O_9S_2 \geq 85\%$), and Nafion ($C_7HF_{13}O_5S.C_2F_4$ 5 wt.%) were obtained from Sigma-Aldrich, Darmstadt, Germany, and used without further purification. Distilled water (DI) was used as a solvent throughout the reaction or otherwise stated.

3.2. Instrumentations and Characterizations

The phase composition and crystallographic structure of the prepared samples were confirmed by X-ray diffraction (XRD) analysis (Cu Kα radiation, λ = 1.5406 Å, PANalytical X'pert Pro, EA Almelo, The Netherlands). The chemical functional groups and bonding were analyzed through Fourier-transform infrared spectroscopy (FT-IR) with KBr pellets and a resolution of 4 cm^{-1} (PerkinElmer, Buckinghamshire, PA, USA), and X-ray photoelectron spectroscopy (XPS, JEOL-JPS-9030, Tokyo, Japan) with standard Mg source. The morphology, microstructure, and elemental composition were examined by field-emission scanning electron microscopy (FE-SEM, JEOL-JSM-7610F, Tokyo, Japan) equipped with energy-dispersive X-ray spectroscopy (EDX, X-MaxN, Oxford Instruments, Abingdon, UK). Optical properties were assessed through UV-visible diffuse reflectance spectroscopy (UV-DRS, Jasco V-770, Tokyo, Japan) and photoluminescence spectroscopy (PL, Micro PL-UniNanoTech, Gyeonggi-do, Republic of Korea) using 266 nm laser excitation. Electrochemical properties were studied via linear sweep voltammetry (LSV), electrochemical impedance spectroscopy (EIS), and Mott–Schottky analysis (Autolab PGSTAT128N-FRA32M, Livonia, MI, USA).

3.3. Synthesis of Pristine g-C$_3$N$_4$ (g-CN) and Sulfonic acid-Functionalized g-C$_3$N$_4$ (SA-g-CN)

The graphitic carbon nitride (g-CN) was synthesized by a thermal polycondensation reaction using dicyandiamide as a precursor material. Briefly, 4 g of dicyandiamide was placed in a silica crucible with the lid after being finely ground and heated in a muffle

furnace at 550 °C for 3 h with a heating ramp of 5 °C/min. The pale-yellow g-CN was obtained and stored for further reactions. Secondly, 1 g of bulk g-CN was added to the glass bottle containing 0.1 M H_2SO_4 and stirred at 50 °C until all the solvents were evaporated by the total solvent evaporation (TSE) technique. Later, the obtained powder was heated at 200 °C for 2 h to strengthen the $N-SO_3H$ bond and SA-g-CN was obtained for further applications.

3.4. Synthesis of Pristine BiOI, g-CN/BiOI and SA-g-CN/BiOI Nanocomposites

The solvothermal method was employed for the synthesis of BiOI nanoplates. A volume of 100 mmol of $Bi(NO_3).6H_2O$ and 0.2 M of potassium iodide was added to 1:1 ethylene glycol and distilled water mixture (80 mL) and stirred vigorously until the homogenous mixture was obtained. After that, the homogenous solution was added to the Teflon-lined autoclave and placed in the muffle furnace at 140 °C for 10 h. The obtained product was washed with DI and ethanol multiple times and dried overnight in a hot-air oven at 60 °C.

The nanocomposites were prepared by the total solvent evaporation (TSE) technique, and for this, equal amounts of g-CN, SA-g-CN and BiOI were added to the bottle containing 10 mL of methanol and kept for magnetic stirring at 60 °C until thorough solvent vaporization. Then, the obtained g-CN/BiOI and SA-g-CN/BiOI were dried overnight in a hot-air oven and utilized for further analyses and applications.

3.5. Photo(electro)chemical Measurements and Photocatalytic Applications

The photocatalytic oxidation of tartrazine (TTZ) was performed using pristine and composite materials. All the degradation reactions were carried out using a 350 W Xenon arc lamp with AM 1.5G filter (100 mW/cm^2) obtained from Enlitech (ALS-300-G2), Taiwan, and the photoreactor was placed vertically about 40 cm from the light source. In this study, for the photocatalytic oxidation of TTZ dye, 50 mL (0.010 g L^{-1}) was added with 25 mg of catalyst and bath-sonicated for even dispersion of the photocatalyst. The photocatalytic reactor was made of a double-walled Pyrex beaker with a water circulatory system to retain the optimum temperature throughout the experiment (24 ± 1 °C). After 15 min under stirring in dark conditions, the reactor was placed in the light source and the 3 mL aliquots were collected at regular intervals to determine the percentage of degradation using a UV-Vis spectrophotometer.

The Mott–Schottky plots were measured using a Metrohm Autolab potentiostat/galvanostat (FRA32M module integrated with NOVA). The electrochemical impedance spectroscopy (EIS) and the transient photocurrent (TPC) measurements were obtained using the electrochemical workstation (CHI1205B). For the Mott–Schottky measurements, 0.1 M Na_2SO_4 was used as an electrolyte. And for the photocurrent and EIS measurements, 0.1 M NaOH and 5 mM $[Fe(CN)_6]^{3-/4-}$ mixture dispersed in 100 mM KCl were used as electrolyte solutions, respectively. In these analyses, Ag/AgCl (sat. KCl), a platinum wire, and a sample-coated indium tin oxide (ITO) plate were used as reference, counter, and working electrodes, respectively. The working electrode was prepared by cleaning the required ITO plates using acetone, ethanol, and deionized water, followed by drop casting the 50 μL of sample solution (i.e., 5 mg of photocatalysts dispersed in 1 mL DI/IPA mixture). The photo(electro)chemical oxygen evolution reactions (OER) were carried out using the same three-electrode system using 0.1 M Na_2SO_4/0.1 M Na_2SO_3 as the electrolyte solution.

4. Conclusions

In summary, this study successfully demonstrated the fabrication of a high-performance Z-scheme heterojunction photo(electro)catalyst by integrating sulfonic acid-modified graphitic carbon nitride (SA-g-CN) with bismuth oxyiodide (BiOI). The resulting composite exhibited exceptional photocatalytic activity, achieving 98.26% degradation of tartrazine within 60 min of irradiation. Concurrently, the catalyst demonstrated promising photo-electrochemical water oxidation performance, with an OER onset potential of 0.94 V (vs.

Ag/AgCl) and a high photocurrent density of 6.04 mA. The synergistic interplay between SA-g-CN and BiOI, facilitated by the formation of a Z-scheme heterojunction, effectively promoted charge separation, and suppressed recombination, leading to enhanced catalytic efficiency. The incorporation of sulfonic acid functional groups further improved charge carrier dynamics and expanded the light absorption range. This research underscores the potential of SA-g-CN/BiOI as a versatile and efficient photocatalyst for addressing environmental and energy-related challenges. Future studies could explore the optimization of catalyst composition and structure to further enhance performance and expand its application scope.

Supplementary Materials: The following supporting information can be downloaded at: https://www.mdpi.com/article/10.3390/inorganics12090243/s1, Figure S1: XPS core-level spectra of S 2p of SA-g-CN; Figure S2: XRD diffraction pattern (a) and FTIR spectrum of recycled SA-g-CN/BiOI heterojunction nanocomposite after five successive reaction cycles (b); Figure S3: FESEM images of the recycled SA-g-CN/BiOI composite (a,b).

Author Contributions: Conceptualization, S.B., H.V. and T.C.-K.Y.; methodology, S.B., H.V. and C.-C.W.; software, S.B., H.V. and C.-C.W.; validation, S.B., J.C.J. and T.C.-K.Y.; formal analysis, S.B., H.V. and C.-C.W.; investigation, S.B., H.V. and J.C.J.; resources, J.C.J. and T.C.-K.Y.; data curation, S.B. and H.V.; writing—original draft preparation, S.B. and H.V.; writing—review and editing, S.B., J.C.J. and T.C.-K.Y.; supervision, J.C.J. and T.C.-K.Y.; project administration, T.C.-K.Y.; funding acquisition, J.C.J. and T.C.-K.Y. All authors have read and agreed to the published version of the manuscript.

Data Availability Statement: The data presented in this study are available on request from the corresponding author. The data are not publicly available due to ongoing research and analysis.

Conflicts of Interest: The sponsors had no role in the design, execution, interpretation, or writing of the study.

References

1. Yao, S.; He, J.; Gao, F.; Wang, H.; Lin, J.; Bai, Y.; Fang, J.; Zhu, F.; Huang, F.; Wang, M. Highly Selective Semiconductor Photocatalysis for CO_2 Reduction. *J. Mater. Chem. A* **2023**, *11*, 12539–12558. [CrossRef]

2. Jabbar, Z.H.; Esmail Ebrahim, S. Recent Advances in Nano-Semiconductors Photocatalysis for Degrading Organic Contaminants and Microbial Disinfection in Wastewater: A Comprehensive Review. *Environ. Nanotechnol. Monit. Manag.* **2022**, *17*, 100666. [CrossRef]

3. Idris, A.M.; Liu, T.; Shah, J.H.; Zhang, X.; Ma, C.; Malik, A.S.; Jin, A.; Rasheed, S.; Sun, Y.; Li, C.; et al. A Novel Double Perovskite Oxide Semiconductor Sr_2CoWO_6 as Bifunctional Photocatalyst for Photocatalytic Oxygen and Hydrogen Evolution Reactions from Water under Visible Light Irradiation. *Sol. RRL* **2020**, *4*, 1900456. [CrossRef]

4. Balu, S.; Venkatesvaran, H.; Lan, K. Photo (Electro) Catalyst for PEC Oxygen Evolution Reaction and Removal of Tetracycline. *Catalysts* **2022**, *12*, 1601. [CrossRef]

5. Balu, S.; Chen, Y.L.; Chen, S.W.; Yang, T.C.K. Rational Synthesis of $BixFe_1-xVO_4$ Heterostructures Impregnated Sulfur-Doped g-C_3N_4: A Visible-Light-Driven Type-II Heterojunction Photo(Electro)Catalyst for Efficient Photodegradation of Roxarsone and Photoelectrochemical OER Reactions. *Appl. Catal. B Environ.* **2022**, *304*, 120852. [CrossRef]

6. Xing, F.; Zeng, R.; Cheng, C.; Liu, Q.; Huang, C. POM-Incorporated $ZnIn_2S_4$ Z-Scheme Dual-Functional Photocatalysts for Cooperative Benzyl Alcohol Oxidation and H2 Evolution in Aqueous Solution. *Appl. Catal. B Environ.* **2022**, *306*, 121087. [CrossRef]

7. Shang, W.; Li, Y.; Huang, H.; Lai, F.; Roeffaers, M.B.J.; Weng, B. Synergistic Redox Reaction for Value-Added Organic Transformation via Dual-Functional Photocatalytic Systems. *ACS Catal.* **2021**, *11*, 4613–4632. [CrossRef]

8. Balu, S.; Velmurugan, S.; Palanisamy, S.; Chen, S.-W.; Velusamy, V.; Yang, T.C.K.; El-Shafey, E.-S.I. Synthesis of α-Fe_2O_3 Decorated g-C_3N_4/ZnO Ternary Z-Scheme Photocatalyst for Degradation of Tartrazine Dye in Aqueous Media. *J. Taiwan Inst. Chem. Eng.* **2019**, *99*, 258–267. [CrossRef]

9.   Kaya, S.I.; Cetinkaya, A.; Ozkan, S.A. Latest Advances on the Nanomaterials-Based Electrochemical Analysis of Azo Toxic Dyes Sunset Yellow and Tartrazine in Food Samples. *Food Chem. Toxicol.* **2021**, *156*, 112524. [CrossRef]

10. Haridevamuthu, B.; Murugan, R.; Seenivasan, B.; Meenatchi, R.; Pachaiappan, R.; Almutairi, B.O.; Arokiyaraj, S.; K, K.M.; Arockiaraj, J. Synthetic Azo-Dye, Tartrazine Induces Neurodevelopmental Toxicity via Mitochondria-Mediated Apoptosis in Zebrafish Embryos. *J. Hazard. Mater.* **2024**, *461*, 132524. [CrossRef]

11. Russo, A.V.; Merlo, B.G.; Jacobo, S.E. Adsorption and Catalytic Degradation of Tartrazine in Aqueous Medium by a Fe-Modified Zeolite. *Clean. Eng. Technol.* **2021**, *4*, 100211. [CrossRef]

12. Wouters, R.D.; Muraro, P.C.L.; Druzian, D.M.; Viana, A.R.; de Oliveira Pinto, E.; da Silva, J.K.L.; Vizzotto, B.S.; Ruiz, Y.P.M.; Galembeck, A.; Pavoski, G.; et al. Zinc Oxide Nanoparticles: Biosynthesis, Characterization, Biological Activity and Photocatalytic Degradation for Tartrazine Yellow Dye. *J. Mol. Liq.* **2023**, *371*, 121090. [CrossRef]

13. Zhang, S.; Saeeda; Khan, A.; Ali, N.; Malik, S.; Khan, H.; Ali, N.; Iqbal, H.M.N.; Bilal, M. Designing, Characterization, and Evaluation of Chitosan-Zinc Selenide Nanoparticles for Visible-Light-Induced Degradation of Tartrazine and Sunset Yellow Dyes. *Environ. Res.* **2022**, *213*, 113722. [CrossRef]

14. Soufi, A.; Hajjaoui, H.; Elmoubarki, R.; Abdennouri, M.; Qourzal, S.; Barka, N. Heterogeneous Fenton-like Degradation of Tartrazine Using $CuFe_2O_4$ Nanoparticles Synthesized by Sol-Gel Combustion. *Appl. Surf. Sci. Adv.* **2022**, *9*, 100251. [CrossRef]

15. Bharagav, U.; Ramesh Reddy, N.; Nava Koteswara Rao, V.; Ravi, P.; Sathish, M.; Rangappa, D.; Prathap, K.; Shilpa Chakra, C.; Shankar, M.V.; Appels, L.; et al. Bifunctional $G-C_3N_4$/Carbon Nanotubes/WO_3 Ternary Nanohybrids for Photocatalytic Energy and Environmental Applications. *Chemosphere* **2023**, *311*, 137030. [CrossRef]

16. Venkatesvaran, H.; Balu, S.; Tsai, B.-S.; Yang, T.C.-K. Construction of Z-Scheme Heterojunction Based on BiOBr-Nanoflakes Embedded Sulfonic-Acid-Functionalized $g-C_3N_4$ for Enhanced Photocatalytic Removal of Hazardous Pollutants in Aqueous Media. *J. Taiwan Inst. Chem. Eng.* **2023**, *142*, 104637. [CrossRef]

17. Velusamy, P.; Liu, X.; Sathiya, M.; Alsaiari, N.S.; Alzahrani, F.M.; Nazir, M.T.; Elamurugu, E.; Pandian, M.S.; Zhang, F. Investigate the Suitability of $G-C_3N_4$ Nanosheets Ornamented with BiOI Nanoflowers for Photocatalytic Dye Degradation and PEC Water Splitting. *Chemosphere* **2023**, *321*, 138007. [CrossRef]

18. Zhu, P.; Luo, D.; Liu, M.; Duan, M.; Lin, J.; Wu, X. Flower-Globular $BiOI/BiVO_4/g-C_3N_4$ with a Dual Z-Scheme Heterojunction for Highly Efficient Degradation of Antibiotics under Visible Light. *Sep. Purif. Technol.* **2022**, *297*, 121503. [CrossRef]

19. Venkatesvaran, H.; Balu, S.; Chowdhury, A.; Chen, S.; Yang, T.C. Photo–Redox Properties of $–SO_3H$ Functionalized Metal-Free $g-C_3N_4$ and Its Application in the Photooxidation of Sunset Yellow FCF and Photoreduction of Cr (VI). *Catalysts* **2022**, *12*, 751. [CrossRef]

20. Luo, Y.; Liu, Z.; Liu, J.; Cai, W.; Liao, Z.; Feng, X.; Zheng, J.; Zhang, C.; Fang, Y. Adjustable N→π* Electronic Transition by Sulfonated Benzene Functionalized $G-C_3N_4$ for Enhanced Photocatalytic H_2 Generation. *Int. J. Hydrogen Energy* **2024**, *64*, 558–568. [CrossRef]

21. Nayebi, M.; Faraji, A.; Bahadoran, A.; Othman, Z.J.; Arghavani, S.; Kargar, P.G.; Sajjadinezhad, S.M.; Varma, R.S. TiO_2/g-C_3N_4/$SO_3H(IL)$: Unique Usage of Ionic Liquid-Based Sulfonic Acid as an Efficient Photocatalyst for Visible-Light-Driven Preparation of 5-HMF from Cellulose and Glucose. *ACS Appl. Mater. Interfaces* **2023**, *15*, 8054–8065. [CrossRef] [PubMed]

22. Sun, X.; He, K.; Chen, Z.; Yuan, H.; Guo, F.; Shi, W. Construction of Visible-Light-Response Photocatalysis-Self-Fenton System for the Efficient Degradation of Amoxicillin Based on Industrial Waste Red Mud/CdS S-Scheme Heterojunction. *Sep. Purif. Technol.* **2023**, *324*, 124600. [CrossRef]

23. Pan, J.; Wang, P.; Wang, P.; Yu, Q.; Wang, J.; Song, C.; Zheng, Y.; Li, C. The Photocatalytic Overall Water Splitting Hydrogen Production of $G-C_3N_4$/CdS Hollow Core–Shell Heterojunction via the HER/OER Matching of Pt/MnOx. *Chem. Eng. J.* **2021**, *405*, 126622. [CrossRef]

24. Balu, S.; Chen, S.-W.; Piskunov, S.; Venkatesvaran, H.; Lee, L.W.-C.; Yang, T.C.-K. In-Co-Doped $Bi_{1-X}VO_4$ Drenched Sulfur–Doped $g-C_3N_4$ Nanocomposite: A Type-II Photo(Electro)Catalytic System for Visible-Light–Driven Water-Splitting and Toxic Removal Applications. *Adv. Compos. Hybrid Mater.* **2024**, *7*, 32. [CrossRef]

25. Takata, T.; Jiang, J.; Sakata, Y.; Nakabayashi, M.; Shibata, N.; Nandal, V.; Seki, K.; Hisatomi, T.; Domen, K. Photocatalytic Water Splitting with a Quantum Efficiency of Almost Unity. *Nature* **2020**, *581*, 411–414. [CrossRef]

26. NavakoteswaraRao, V.; Shankar, M.V.; Yang, B.L.; Ahn, C.W.; Yang, J.M. Effective Excitons Separation in Starfish Bi_2S_3/TiO_2 Nanostructures for Enhanced Hydrogen Production. *Mater. Today Chem.* **2022**, *26*, 101096. [CrossRef]

27. Chowdhury, A.; Balu, S.; Venkatesvaran, H.; Chen, S.-W.; Yang, T.C.-K. Facile Construction of $CuFe_2O_4$/p-g-C_3N_4 p-n Heterojunction with Boosted Photocatalytic Activity and Sustainability for Organic Degradation Reactions under Visible-Light. *Surf. Interfaces* **2022**, *34*, 102329. [CrossRef]

28. Vahabirad, S.; Nezamzadeh-Ejhieh, A.; Mirmohammadi, M. The Coupled $BiOI/(BiO)_2CO_3$ Catalyst: Brief Characterization, and Study of Its Photocatalytic Kinetics. *J. Solid State Chem.* **2022**, *314*, 123405. [CrossRef]

29. Li, Y.; He, J.; Wang, X.; Zhao, J.; Liu, R.; Liu, Y.; Li, F. Introduction of Crystalline Hexagonal-C_3N_4 into $g-C_3N_4$ with Enhanced Charge Separation Efficiency. *Appl. Surf. Sci.* **2021**, *559*, 149876. [CrossRef]

30. Liang, D.; Wu, J.; Xie, C.; Wen, J.; Lyu, Y.; Sofer, Z.; Zheng, J.; Wang, S. Efficiently and Selectively Photocatalytic Cleavage of CC Bond by C_3N_4 Nanosheets: Defect-Enhanced Engineering and Rational Reaction Route. *Appl. Catal. B Environ.* **2022**, *317*, 121690. [CrossRef]

31. Mehralipour, J.; Darvishali, S.; Bagheri, S.; Kermani, M. Photocatalytic-Ozonation Process in Oxytetracycline Degradation in Aqueous Solution: Composite Characterization, Optimization, Energy Consumption, and by-Products. *Sci. Rep.* **2023**, *13*, 11113. [CrossRef] [PubMed]
32. Zhu, D.; Zhou, Q. Nitrogen Doped G-C$_3$N$_4$ with the Extremely Narrow Band Gap for Excellent Photocatalytic Activities under Visible Light. *Appl. Catal. B Environ.* **2021**, *281*, 119474. [CrossRef]
33. Chowdhury, A.; Balu, S.; Yang, T.C.-K. Construction of α-Fe$_2$O$_3$-NPs@AgVO$_3$-NRs Z-Scheme Heterojunction: An Efficient Photo(Electro)Catalyst for Cr(VI) Reduction and Oxygen Evolution Reactions under Visible-Light. *J. Environ. Chem. Eng.* **2023**, *11*, 109769. [CrossRef]